

# Unraveling the control of cell cycle periods during intestinal stem cell differentiation

Richard Ballweg<sup>1</sup>, Suengwon Lee<sup>1</sup>, Xiaonan Han<sup>2</sup>, Philip Maini<sup>3</sup>, Helen Byrne<sup>3</sup>, Christian I Hong<sup>1,4,5</sup>, and Tongli Zhang<sup>1\*</sup>

1. Department of Pharmacology and Systems Physiology, College of Medicine, University of Cincinnati, Cincinnati, OH
2. Division of Gastroenterology, Hepatology, and Nutrition, Cincinnati Children's Hospital, Cincinnati, OH and Key Laboratory of Human Disease Comparative Medicine, Health Ministry; Institute of Laboratory Animal, Chinese Academy Institute of Science (CAMS) and Peking Union Medical College (PUMC)
3. Wolfson Centre for Mathematical Biology, Mathematical Institute, University of Oxford, Oxford, United Kingdom
4. Division of Developmental Biology, Cincinnati Children's Hospital Medical Center, 3333 Burnet Ave, Cincinnati, OH
5. Center for Stem Cell and Organoid Medicine, Cincinnati Children's Hospital Medical Center, 3333 Burnet Ave, Cincinnati, OH

\* Correspondence should be addressed to Tongli.Zhang@uc.edu

Running Title: Modeling stem cell proliferation

## Abstract

During differentiation, intestinal stem cells (ISCs), a prototypical adult stem cell pool, become either secretory [transit-amplifying](#) cells (sTAs), which give rise to all secretory cell types, or absorptive [transit amplifying](#) cells (aTAs), which give rise to enterocytes. These cells exhibit distinct cell cycle dynamics: ISCs cycle with a period of 24 hrs, aTAs with a period of about 12 hrs, while sTAs arrest their cycle. The cell cycle dynamics of ISCs and their progeny are [a](#) systems level [property that](#) emerges [from](#) interactions between the cell cycle control machinery and multiple regulatory pathways. Though many mathematical models have been developed to study the details of the cell cycle and related regulatory pathways, few models have been constructed to unravel the dynamic consequences of their interactions. To fill this gap, we present a simplified model focusing on the interaction between four key regulatory pathways (STAT, Wnt, [Notch](#), and MAPK) and cell cycle control. After experimentally validating [a](#) model prediction, [which showed](#) that the [Notch](#) pathway can fine-tune the cell cycle period, we perform further model analysis which reveals that the change of cell cycle period accompanying ISC differentiation is likely controlled by a design principle that has been well studied in dynamical systems theory, a Saddle Node on Invariant Circle (SNIC) bifurcation. [Given that the mechanisms which control the cell cycle are conserved in most eukaryotic cell types](#), this general principle potentially controls the interplay between proliferation and differentiation for a broad range of stem cells.

## Introduction

Stem cells are characterized by their distinct ability to both proliferate and differentiate, and can be broadly classified into two types: embryonic stem cells, which give rise to the three germ layers during embryonic development; and adult (somatic) stem cells which reside in a number of adult tissues, where they serve as a lifelong source of cells that can regenerate damaged tissues and replenish dying cells (1, 2). Intestinal stem cells (ISCs) represent a prototypical adult stem cell pool that reside in niches at the base of intestinal crypts (2) (left panel, **Figure 1A**). The differentiation of these cells and their progenitors continuously repopulate the epithelial layer of the intestine, while the active proliferation of ISCs allows for the prolonged maintenance of the stem cell pool (2).

Differentiation of ISCs is associated with a change in their proliferation dynamics (right panel, **Figure 1A**). When they differentiate, ISCs make a binary fate decision to become either absorptive transit-amplifying cells (aTA) or secretory transit-amplifying cells (sTA) (3). ISCs have been estimated to proliferate with a period of about 24 hours(4, 5); while their daughter cells either cycle with a shorter period of 12 hours (aTAs) (4), or exit the cell cycle (sTAs) (6). Such experimental observations trigger an intriguing question: how do these stem cells alter their proliferation rates during the differentiation process?

To uncover the dynamical control of proliferation during ISC differentiation, we have developed a simple mathematical model that includes a number of key signaling pathways (Wnt, Notch, and MAPK), which have been shown experimentally to be critical regulators of proliferation and differentiation in ISCs (2). These regulatory pathways were then coupled to the cell cycle control network to gain insights into how their interplay influences the cell cycle (**Figure 1**). Using this simplified model, we are able to recapture the experimentally observed proliferation dynamics of

ISCs and their progenitors which arise during the differentiation process. Rigorous analysis of the model with a diverse set of tools revealed that a simple dynamic scenario, in terms of a well-defined Saddle Node of Invariant Circle (SNIC) bifurcation, might underlie the dramatic changes of cell proliferation during the differentiation of ISCs. In addition, the model also predicts how the proliferation of ISCs is disrupted by alterations in the STAT signaling pathway that are present in Inflammatory Bowel Disease (IBD) (7).

This work illustrates that simplified theoretical models can be used to unravel complex biological control mechanisms. The cell cycle dynamics of eukaryotic cells are controlled by conserved cell cycle regulators (Cdks, Cyclins, Cdk inhibitors etc.) and the feedbacks between them (8). Hence, we believe that this simplified model could be used to study a host of other types of stem cells such as embryonic or hematopoietic stem cells which alter their proliferation rates during differentiation (9, 10) .

## METHODS

### Modeling approach

When developing our mathematical model, we adopt a generic approach in which the dynamics of a particular model component,  $X_i$  are determined by the following ODE:

$$\frac{dX_i}{dt} = \tau_i (F_i - X_i)$$

Where in

$$F_i = \frac{1}{1+e^{-\sigma W_i}} \text{ and } W_i = R_0^i + \sum_j R_j^i \cdot X_j$$

Briefly, each model component ( $X_i$ ) reaches its desired steady ( $F_i$ ) over time scale ( $\tau$ ). The steady state of each model component ( $F_i$ ) is a nonlinear function of a weighted sum ( $W_i$ ) over all model components  $X_j$  ( $j \neq i$ ). Positive weights ( $R_j^i > 0$ ) promote  $X_i$ , while negative weights ( $R_j^i < 0$ ) inhibit  $X_i$ . Weights of zero ( $R_j^i = 0$ ) correspond to model components which have no effect on  $X_i$ . A more detailed description of the approach can be found in the literature (11, 12) as well as in our previous publications (13) and (14).

Existing experimental observations suggest that the cell cycle periods are controlled by the signaling gradients in the crypt. For example, WNT proteins are believed to form a gradient with highest levels in the crypt base (in the stem cell niche) and lowest levels near the top of the crypt (15); a MAPK gradient is thought to run in the opposite direction (16). ISCs reside near the crypt base where they receive high levels of WNT and lower levels of MAPK. As such, cells in this environment should cycle with a period of  $\sim 24$  hours. As cells move up the crypt and into the TA

zone, they should begin to cycle faster with a period of  $\sim 12$  hours (4). In order to recapture these biological observations, we first manually estimated a single set of parameters that could recapture these dynamics, and this served as the basal parameter set. The governing equations and the basal parameter values for the current models are shown in **Supplementary Tables 1 and 2**. Differential equations were simulated using XPPAUT (<http://www.math.pitt.edu/~bard/xpp/xpp.html>) and plotted using python (<https://www.python.org/>).

To produce a population of models, parameters for each model were randomly chosen from a uniform distribution that ranged from between 70% to 130% of their basal values. Due to the simplifications of the cell cycle control module, the parameters controlling the interactions between CDK and C20 were not allowed to vary nor were the strengths of the interactions between CCS, CKR and CDK. For the environmental variables (WNT, MAPK and DSL), a value was chosen from randomly from a uniform distribution over the range [0,2].

An Approximate Bayesian Computation (ABC) rejection scheme (17) was used to identify feasible parameter sets. For a given model (i.e a given parameter set), if simulation of the parameter set satisfied any of our pre-set criteria ( $CCT > 20$  hrs,  $CCT < 18$  hrs or Cell Cycle arrest), then the parameter set was saved. If the parameter set did not meet any of these criteria, then the parameter set was rejected. This process continued until a desired number of parameter sets was amassed for each of the three cell types.

Some parameter sets produced cells that arrest with high levels of CDK. Since these do not resemble any known intestinal cells, the corresponding models were not used in any further analyses.

To simulate the cellular response to inflammation, representative cells were first chosen and simulated. Then, an addition of IL-22 was mimicked at hour 40 of the temporal simulation by changing the environment variable IL-22 from 0 to 1.

### **Bifurcation Analysis.**

To perform the one parameter bifurcation analysis, the differential equations for CDK, CKR and C20 were solved with CCS as a control parameter. For the two parameter bifurcation analysis, both CCS and ATOH1 were viewed as control parameters, and the position of the threshold between the oscillatory and the non-oscillatory regions was tracked with Oscill8 (<http://oscill8.sourceforge.net>). All bifurcation diagrams were plotted with Python (<https://www.python.org/>).

### **Classification Tree Analysis**

Each simulation was binned into one of 3 groups based on its cell cycle time; Fast ( $CCT < 18$  hrs), Slow ( $CCT > 20$  hrs) or Arrested ( $CCT = 0$ ). These groups were then used as classifiers for tree analyses. Tree models were run using the model parameters in addition to the steady state values for model components which were not shown to oscillate. Trees were computed in R (<https://www.r-project.org/>) using the rpart2 algorithm within the caret package (18).

### **Random Forest Analysis**

Groups (as defined above) were used as classifiers for the Random Forest analysis. Computation was done in R using the randomForest algorithm (19) within the caret package (18). Default settings were used along with 10-fold cross-validation. The most accurate model, defined as the model with the lowest mis-classification rate, was chosen to calculate variable importance, which

is a measure of the reduction in the accuracy of the statistical model when each of the predictors is permuted. This is done by permuting the value of each parameter and calculating the difference between the out of bag error for the initial model and the permuted model. This difference is then averaged over all trees within the forest and normalized by the standard error. The resulting error values are scaled to the maximum error value, so that predictors with a value of 100 are the most important predictors within the statistical model and predictors with a value of 0 have no importance in the model (18).

Both the number of models and the parameter variations included in the models influence the results of the CART and Random Forest analyses. To address these effects, we performed additional simulations in which either the number of models increased (12,000 total models) or decreased (3,000 total models). We also carried out simulations in which the parameter ranges were varied. See **Supplementary Figure 2A –D** (CART Analysis) and **Supplementary Figure 3A-D** (Random Forest Analysis).

### **Confocal imaging and analysis**

The imaging data from control and *Atoh1* deficient enteroids (Matsu-ura et al, 2016) were processed using ZEN (Zeiss, Thornwood, NY) or NIS elements (Nikon, Melville, NY). 3D images were reconstructed and analyzed using IMARIS (Bitplane, Zurich, Switzerland) to quantify the duration of fluorescent intensity in crypt structures.

Histogram distributions and Student's t-test (significance level  $p=0.05$ ) were conducted using Prism 6 (GraphPad software, La Jolla, CA) and SigmaPlot (Systat Software, San Jose, CA).

## Results

### Diverse parameter sets allow a single model structure to recapture the proliferation dynamics of ISC, aTA and sTA cells

Our mathematical model comprises four interacting modules representing: the STAT signaling pathway, the [WNT/MAPK pathways](#), the Notch signaling pathway, and the cell cycle (**Figure 1B**). The cell cycle module has been reduced to its core components. CDK levels are controlled via two interactions: a negative feedback formed by CDK and its repressor [APC/CDC20](#) (C20); and a mutually antagonistic positive feedback that exists between CDK and a generic class of cell cycle repressors (CKR), which represent the action of many repressors of the cell cycle (i.e. p21, p27, p57). CKR is also inhibited by cell cycle starters (CCS), which represent the net effect of cell cycle promoters ( i.e. CyclinD, cMyc), which are activated by upstream signaling pathways such as the [Wnt](#) or [MAPK](#) pathways. [Both WNT and MAPK can promote cell proliferation \(20\) and the downstream transcriptional activities of these two pathways are hypothesized to repress each other in a mutually-antagonistic feedback \(21, 22\).](#) The STAT signaling pathway, which plays a significant role in the pathogenesis of [IBD](#), is assumed to activate CCS through inflammatory signals (23, 24). The Notch signaling pathway represses CDK inhibitors through its inhibition of [ATOH1, thus promoting](#) cell proliferation in response to Delta/Serrate/LAG-2 ligands ([DSL](#)) (25). A detailed description of these modules is available in the **Supplementary Text**.

The molecular interactions contained within the modules were translated into a system of ordinary differential equations (ODEs, **Supplementary Table 1**), and parameter sets (which [yield](#) experimentally observed cell cycle periods) were chosen at random (elaborated in **Methods**). With differing parameter sets, the model structure could reproduce the characteristic proliferation dynamics of ISCs, aTAs, and sTAs. Some parameter sets mimic intestinal stem cell dynamics with

a 24 hour period of proliferation (see **Figure 2A** for three examples); others exhibit a 12 hour proliferation rate similar to aTAs (see **Figure 2B**). A third group of models do not exhibit proliferative (oscillatory) dynamics, and instead reach a stable steady with low CDK which is characteristic of sTAs (simulations not shown). Since the population of models recapitulate the proliferation dynamics of stem and TA cells, we intend to use them as functional “*in silico*” representations of the cell types of interest. However before we may use them for such a purpose, we must first understand how the molecular network can give rise to such drastic differences in proliferation rates of intestinal cells, and second, we must investigate whether these models show similar properties when compared to their experimental counterparts.

### **The simplified models indicate that ATOH1 contributes significantly to the control of cell proliferation**

As an initial test of model quality, we subject our population of models to a classification and regression tree (CART) (26) analysis to understand how individual elements of the molecular control network in our model might contribute to cell cycle periods. Bearing the same structure but different parameter values, our models are characterized by three different types of cell cycle dynamics: fast (<18hr period), slow (>20 hr period), or arrested. Meanwhile, six model components (ATOH1, CCS,  $\beta$ -Catenin, HES1, NOTCH and AP1) reach non-oscillatory steady states. For a comprehensive analysis, all 35 model parameters and the six model components that reach non-oscillatory steady states are analyzed using the CART algorithm.

With recursive partitioning (26), the algorithm finds optimal predictors (parameter values or steady state values) which can classify models. The models are then splint into leaves (nodes or clusters) with similar identities. The resulting Classification Tree divides 6,000 models in a binary fashion (**Figure 2C**). All models are included in the root node (1<sup>st</sup> red node on the top, **Figure 2C**). It

comprises 33% arrested cells, 33% rapidly cycling cells and 33% slowly cycling cells, and is labeled as “arrested” by the software. Then, at a threshold level of *Atoh1* ( $ATOHI \geq 0.38$ ), the root node is divided into two daughter nodes. All models with  $ATOHI \geq 0.38$  are binned into a node that is characterized by a high percentage (91%) of arrested cells (red node, **Figure 2C**). In contrast, models with  $ATOHI < 0.38$  are incorporated into a second node with a high percentage (45%) of fast cycling cells. These two nodes are also labelled on the basis of the dominant cell type. The algorithm continues to divide the resulting nodes in a similar manner until a preset threshold is met. This single tree has a classification accuracy of more than 70%, meaning that given the steady state values of CCS and *ATOHI*, the tree can correctly classify the cell cycle dynamics of more than 70% of cells.

In theory, splitting can continue until leaves contain only models of homogeneous behaviors (example tree, **Supplementary Figure 1**). Growing a tree in this way comes with a number of costs; the trees can be difficult to visualize, hard to interpret and are vastly overfit. So for practical purposes, trees are pruned to a smaller size to aid with visualization and to prevent overfitting (**Figure 2C**).

To overcome the limitations brought on by a single classification tree, the Random Forest algorithm was used to achieve collective results from an ensemble of randomly modified trees (i.e. forest) (27). By computing and averaging the consequential error when a single model parameter or component is permuted, the Random Forest was used to calculate the relative importance of each model parameter or component (**Figure 2D**). The Random Forest (RF) analysis revealed that *ATOHI* and CCS, the two model components used for the initial splitting in the classification tree, play critical roles in classifying cell cycle periods. Given the data-driven nature of the CART and Random Forest methods, the results they generate are sensitive to the number of the models

analyzed and the parameter variations included in these models (**Supplementary Figures 2A –D** (CART Analysis) and **Supplementary Figures 3A-D** (Random Forest Analysis)). Despite such variation, these analyses consistently reveal that Atoh1 and CCS play significant roles in regulating the length of cell cycle periods in intestinal cells. In other words, the CART and Random Forest analyses essentially examined the sensitivity of cell cycle dynamics to all changing model components (parameters and variables) and revealed that the cell cycle period is most sensitive to ATOH1 and CCS.

It is reasonable that ATOH1 and CCS were revealed to be the most significant regulators of cell cycle, as CCS is the model component which summarizes the relative abundance of classical cell cycle promoters, and ATOH1 directly promotes the transcription of cell cycle inhibitors (elaboration and references in **Supplementary Text**). On the other hand, variation in parameters associated with upstream regulators of the cell cycle (e.g. HES1) have less of an effect on the cell cycle.

Given that CCS promotes the activation of CDK, it is expected that CCS significantly contributes to the regulation of cell cycle periods. Therefore, we focused on understanding the role of ATOH1 in controlling intestinal stem cell proliferation *in vitro*.

### **Single cell cycle dynamics of enteroids reveal a significant role for **ATOH1** in controlling cell proliferation rates**

Traditionally, the cell cycle times of intestinal crypt cells have been estimated by pulse chase staining with tritiated thymidine, Brdu or Edu (4, 5). These methods have low precision (because it is difficult to measure single cells) and can have poor temporal resolution (cells not sampled often enough). Three-dimensional intestinal enteroids represent a suitable experimental system to

study crypt cell dynamics, as their *in vitro* nature allows for increased precision and resolution of cellular measurements. Formed by the self-organization of intestinal epithelial cells into “*mini guts*”, enteroids contain the [different](#) cell types seen within the *in vivo* crypt (ISCs, TAs, and differentiated cell types) (28). By combining [this](#) 3D culture system with the fluorescent ubiquitination-based cell cycle indicator (FUCCI) system (29), we have developed a framework that allows for measurements of cell cycle periods with high temporal resolution in single [crypt](#) cells (30). In previous work, we have [used](#) this [technique to show](#) that the duration of the G1 phase of the cell cycle has a strong positive correlation with cell cycle time (CCT) [of](#) intestinal stem and progenitor cells (30). [Based on](#) this strong correlation, we measured the duration of the G1 phase in control vs. *Atoh1* knocked down (KD) enteroids to [evaluate](#) the contribution of [ATOH1](#) to cell cycle dynamics, [as](#) proposed by our CART and RF analyses (**Fig 2C & 2D**). Our experimental results show marked differences in the duration of G1 phases between control and *Atoh1*-KD enteroids (**Figure 3B and C**). The average duration of the G1 phase in *Atoh1*-KD enteroids ( $2.284 \pm 0.213$  hour (average  $\pm$  standard error),  $n=81$ ) is significantly reduced when compared to control enteroids ( $6.684 \pm 0.856$  hour,  $n=38$ ,  $p < 0.0001$ ) (**Figure 3D**). These findings are consistent with separate studies [which](#) show that induction of [ATOH1](#) in skin cancer cell lines increases their doubling time (31).

Given the consistency between the experimental results and the theoretically predicted significance of [ATOH1](#), we conclude that the [theoretical](#) models can serve as “*in silico*” representations of the intestinal cells of interest and can be used for further investigation.

### **A SNIC bifurcation controls cell cycle period in differentiating ISCs**

Although ATOH1 and CCS are “*model components*” in the full model, they rapidly attain steady states in time dependent simulations. Hence, their effect on CCT can be understood by treating them as “*control parameters*” of the CDK control system.

To investigate how cell proliferation is controlled by CCS, we performed a one parameter bifurcation analysis using CDK as the representative variable and CCS as the control parameter. CDK was chosen as the representative variable because its oscillatory dynamics give rise to the cell cycle. At low levels of CCS, the cell cycle control system is attracted to a G1-like stable steady state with low levels of CDK. When CCS levels increase above a threshold ( $\approx 0.3$ , **Figure 4A**), the stable steady state collides with an unstable saddle point and disappears. For levels of CCS above the threshold, the cell cycle module evolves to a stable oscillation (**Figure 4A**).

This particular transition from a stable steady state to oscillation, is defined as a saddle node of invariant circle (SNIC) bifurcation (32). Such bifurcations arise when a stable node disappears by colliding with an unstable saddle point, generating an oscillatory solution with a very large period (hence the term invariant circle). As the level of CCS further increases, the system moves away from the SNIC transition and the oscillation period decreases (**Supplementary Figure 4A**). The observed change of period with sustained amplitude distinguishes a SNIC bifurcation from the more widely studied Hopf bifurcation that controls the transition out of the oscillatory region (**Supplementary Figure 4B**) (32).

The level of CCS needed to generate oscillatory behavior is regulated by other model components. Given the significant contribution of ATOH1 in our computational analyses and experimental observations, we performed a two parameter bifurcation analysis, and tracked the position of the SNIC bifurcation and Hopf bifurcation in response to continuous changes in both CCS and ATOH1. In this way, we identified a pair of lines that decompose the two dimensional parameter

plane into three distinct regions: a central region associated with oscillatory solutions which is surrounded by two regions characterized by non-oscillatory solutions (Figure 4B).

### **The SNIC bifurcation explains the altered proliferation dynamics that occur during differentiation**

We plotted model solutions which correspond to slow cycling ISCs, fast cycling aTAs, and arrested sTAs on the two-dimensional plane spanned by CCS and ATOH1 (Figure 4C). Each model resides at a different position on this 2-D plane, and the relationship between the positions of these models and the SNIC bifurcation line (left line Figure 4C) readily explains both the quantitative and qualitative differences between their proliferation dynamics. Quantitatively, the ISCs reside near the threshold and proliferate with a large period of about 24 hours (blue circles, Figure 4C), while the aTAs reside far from the threshold and proliferate with a short period of about 12 hours (green circles, Figure 4C); qualitatively, the sTAs reside outside the oscillatory region (red circles, Figure 4C) and do not proliferate.

The RF analysis (Figure 2D) indicated that cell cycle dynamics are also controlled by the parameter,  $R_{Ato}^{CKR}$ , which specifies the extent to which ATOH1 promotes CKR production.

Different values of  $R_{Ato}^{CKR}$  within individual cells result in different locations of their SNIC bifurcation lines, and, given the relationship between the SNIC bifurcation lines and the cellular position is what determines the cell cycle period for each cell. To visualize this control, we have plotted a series of SNIC bifurcation curves for different values of  $R_{Ato}^{CKR}$  (Supplementary Figure 5). As the level of  $R_{Ato}^{CKR}$  varies, so too do the slopes of the bifurcation curves (Supplementary Figure 5). This indicates that not only are the levels of individual model components (e.g ATOH1) important in determining the dynamics of the system, but so too are the parameters which control

their respective functions (e.g.  $R_{Ato}^{CKR}$ ). When plotted in three-dimensions (**Figure 4D**), we see that CCS, ATOH1, and  $R_{Ato}^{CKR}$  are sufficient to separate the three cell populations. Collectively, these plots reveal how the positions of individual cells relative to the SNIC boundary can explain their different dynamic behaviors.

### **The model predicts three types of proliferation changes in response to STAT activation**

In response to inflammatory signals, innate immune cells secrete cytokines that activate the STAT signaling pathway within ISCs and consequently enhance their proliferation (24). Consistent with this observation, overexpression of STAT has been shown to increase the pool of actively proliferating intestinal stem cells, while its deletion decreased this pool (23).

Given that the STAT pathway promotes the transcription of CyclinD (23), a component of CCS, STAT activation results in a rightward shift of cells on the ATOH1-CCS plane (indicated by arrows in **Figure 5A**).

Increasing CCS causes different effects within individual cells. A stem cell that was quiescent prior to STAT activation may be pushed into the oscillatory region and start to proliferate (black arrow in **Figure 5A**; the corresponding dynamic simulation is shown in **Figure 5C**). Alternatively, if STAT activation is insufficient to drive a quiescent stem cell into the oscillatory region, then the cell remains quiescent (red arrow in **Figure 5A**; the corresponding dynamic simulation is shown in **Figure 5B**). Such heterogeneous responses may explain why, in the experimental setting, only some, but not all, arrested cells resume cycling upon STAT5 activation (23). Cells that are already slowly proliferating are predicted to respond to STAT activation by relocating into the middle of the oscillatory region and cycling more rapidly (blue arrow in **Figure 5B**, corresponding temporal simulation in **Figure 5D**). Following STAT activation, some cycling cells are arrested with high

CDK activity (not shown); these do not resemble any known intestinal cells and are not analyzed further.

STAT activation has been shown to increase the number of total cycling cells (23, 24). In addition, the overall crypt length is shown to be increased and is accompanied by an increase in the size of the TA zone (24). Shorter cell cycle periods following STAT in ISCs represents a novel and testable prediction of our mathematical model

### **Discussion:**

We have shown how a simple mathematical model can be used to understand complex biological control mechanisms and, in doing so, highlighted how mathematical modeling can be used as a powerful tool in biology (33). Like a microscope, a mathematical model has to strike a balance between its field of view (how many pathways should be included) and its magnification (what level of molecular detail should be included). Finding this balance between field of view and magnification is essential and depends on the model's purpose.

Our current model is designed to understand how the proliferation dynamics of intestinal stem cells change during differentiation. Accordingly, our model focuses on interactions between four simple functional modules rather than detailed mechanistic descriptions of each module.

There are, however, many detailed mathematical models of ISCs, some of which have been developed and validated against experimental data (34-37). Additional models can be found in the reviews by Kershaw et al (38), Fletcher et al (39), Carulli et al (40), and by Lloyd-Lewis et al (41). Compared with these models, our model is purposely simplified to unravel the complex dynamics that govern cell proliferation during differentiation. In future work, it would be interesting to assemble these existing models into multi-scale, models and to test whether the predictions

generated by our simplified model are preserved as we vary the level of detail used to describe each module.

All stem cells undergo proliferation and differentiation. To date, Waddington's Valley has been widely used as the dominant metaphor to describe stem cell differentiation. In mathematical terms, Waddington's valley represents a pitch-fork bifurcation (42). Here, we propose that a SNIC bifurcation may explain the change in the proliferation rates of intestinal stem cells during differentiation. As discussed above, this SNIC bifurcation is sufficient to explain many of the experimentally observed differences between ISCs and TA cells: qualitatively, presence inside or outside of the oscillatory region distinguishes the cycling cells of the crypt (ISCs and aTAs) from the non-cycling sTA cells; quantitatively, the distance between an oscillatory cell and the SNIC boundary (left line, **Figure 4B**) can provide insight into the differences between intestinal stem cells (slow cell cycle period) and absorptive TA cells (fast cell cycle period). Meanwhile, it helps us to understand the effect of STAT pathway activation on ISCs and was able to predict a shorter, cell cycle period in these cells which has not been experimentally observed. Previous models have used SNIC bifurcations to explain how cellular mass controls cell cycle oscillations (43). Here, we demonstrate that the same SNIC bifurcation may explain how ISC cell cycle dynamics are controlled by multiple regulatory pathways during differentiation. As the mechanisms that control the cell cycle are highly conserved amongst eukaryotes (8) we anticipate that our model could be tailored to study the interplay between proliferation and differentiation in other stem cell types.

### **Author Contributions**

CH and TZ designed the study; LS carried out the experimental work; RB, LS, XH, CH and TZ analyzed and interpreted the data; RB, PM, HB and TZ analyzed and interpreted the results from

the computational modeling; all authors contributed to writing the manuscript; all authors read and approved the final manuscript.

### **Acknowledgement**

The work is supported by the University of Cincinnati (TZ), [1R21CA227379-01 \(CIH\)](#), and [1R01DK117005-01 \(CIH\)](#). We thank Meridith Anness for critically reading and editing the manuscript; Emma Teal for insightful discussion; and Toru Matsu-ura for the providing Atoh1-KD enteroids. PKM would like to thank the Mathematical Biosciences Institute (MBI) at [the Ohio State University](#), for partially supporting his [contribution to this work](#). MBI receives its funding through the National Science Foundation grant DMS1440386. [We acknowledge core support from the Cincinnati Digestive Disease Center award \(P30DK0789392\)](#).

## Figure Legends

### Figure 1. The proliferative dynamics of intestinal stem cells and transit amplifying cells.

**A.** A schematic illustration of the intestinal crypt **which** is divided into two regions: the stem cell niche and Transit Amplifying (TA) zone. Intestinal stem cells (ISCs), shown in green, reside in **a niche at the base of the crypt where they are** supported by Paneth cells (shown in yellow). The TA cells reside above the ISCs in the TA zone which comprises a heterogeneous population of TA cells: **absorptive** (aTAs) are shown in pink and proliferate, **while** secretory TA cells (sTAs) shown in blue, do not proliferate. Different TA cells can be marked by their expression of **ATOH1**, with sTAs expressing high levels of **ATOH1** and aTAs expressing low **ATOH1**. Both **cell types** derived from ISCs. **B.** The influence diagram of the current model. Solid shapes with names represent the model components; arrows indicate activation; solid circle heads indicate repression. The model consists of four interacting modules.

### Figure 2. The simplified models suggest that **ATOH1** might contribute significantly to the control of cell proliferation.

**A.** Representative CDK activities of three slowly cycling cells. **B.** Representative CDK activities of three rapidly cycling cells. **C.** Classification Tree. Nodes in which slowly cycling cells dominate are colored in blue; those where rapidly dividing cells dominate are **colored** in green; nodes associated with arrested nodes are colored in red. **D.** Variable importance calculation with a Random Forest analysis. Values are scaled from 0 – 100, where predictors with a value of 0 are dispensable for classification and values of 100 indicate the most important **model components or parameters**.

**Figure 3. Experimental observations confirm the significant role of *ATOH1* in controlling cell proliferation.** **A.** Representative crypt images from time-course confocal microscopy of a FUCCI2 derived enteroid. The arrow indicates a single cell that is traced in order to estimate the duration of the G1 phase of the cell cycle. **B.** Distribution of G1 phase durations obtained from FUCCI2 cells in control enteroids. **C.** Distribution of duration of G1 phase obtained from cells in *Atoh1*-KD enteroids. **D** Cells from control enteroids have a significantly longer G1 phase than *Atoh1* deficient FUCCI enteroids ( $p < 0.0001$ ).

**Figure 4. Bifurcation analysis revealed that a SNIC bifurcation controls ISC proliferation**

**A.** One parameter bifurcation analysis showing the control of CDK by CCS. The black solid curve indicates stable steady state solutions, while the black dashed curve indicates unstable steady states. Blue circles indicate the minimum and maximum amplitudes in oscillatory solutions of CDK. **B.** Two parameter bifurcation diagram showing how CCS and *ATOH1* control the dynamics of CDK. The plane is separated into three distinct regions: one oscillatory and two non-oscillatory regions. The positions of different cells on this map determine their proliferative dynamics. **C.** ISCs (blue), aTAs (green), and arrested cells (red) plotted on a two parameter bifurcation diagram. ISCs and aTAs reside within the oscillatory region, while the arrested cells lie outside this region. **D.** Three-dimensional plot of ISCs (blue), aTAs (green), and arrested cells (red), with a third parameter,  $R_{Ato}^{CKR}$ .

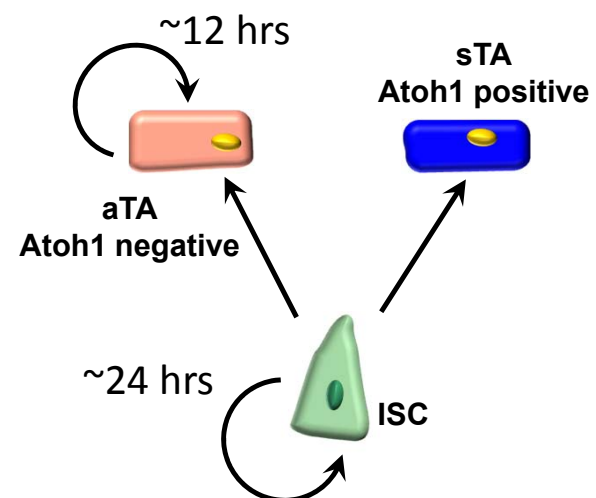
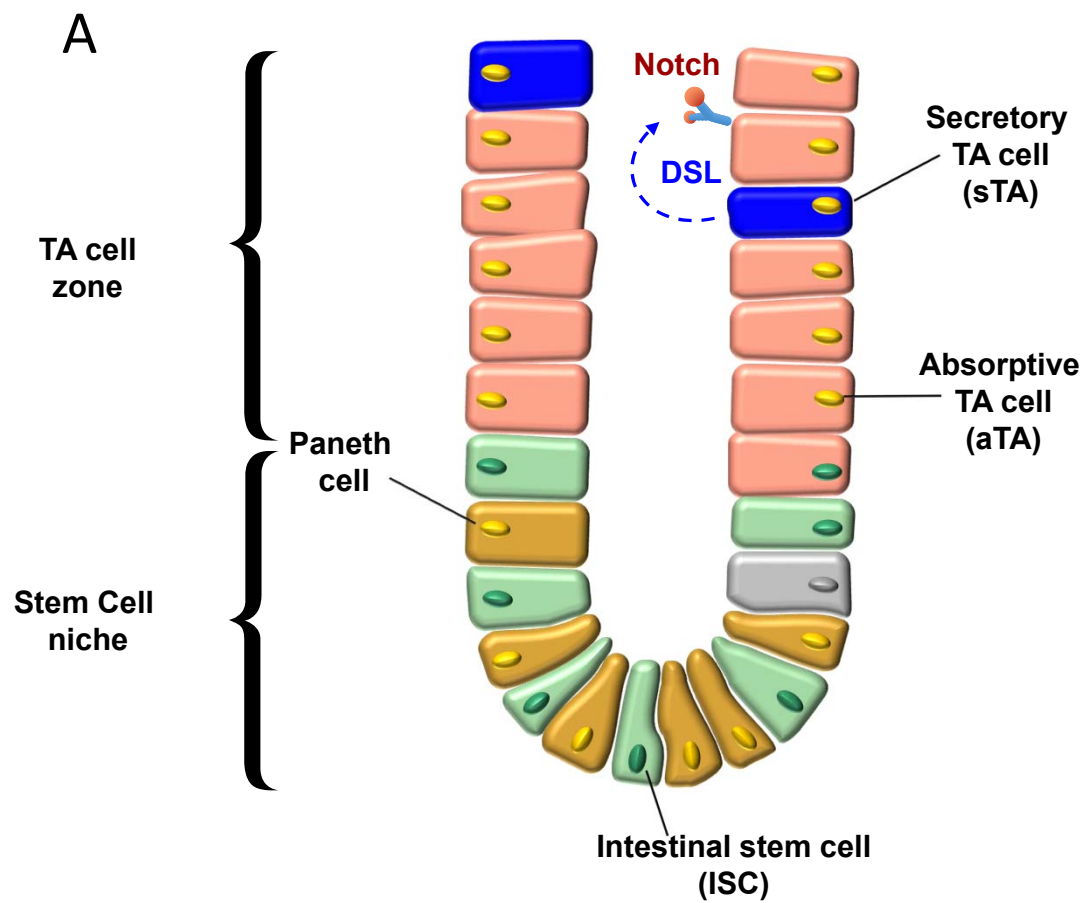
**Figure 5. The model predicts three types of proliferation changes in response to STAT pathway activation.** **A.** The change in intestinal stem cells in response to activation of the STAT pathway. By elevating CCS, activation of the STAT pathway moves the ISCs rightward. Solid circles show the ISCs before STAT activation; open circles of identical colors show these ISCs

after activation of the STAT pathway. The black arrow shows the trajectory of a quiescent ISC that begins cycling following stimulation; the red arrow shows the trajectory of a quiescent cell that remains quiescent following stimulation; the blue arrow shows the trajectory of a cycling ISC that oscillates faster following STAT activation. **B-D.** Time series simulations of cells before and after STAT activation (black dotted line); a cell that remains arrested following activation (**B**), a cell begins to proliferate upon activation (**C**), a third cell proliferates faster following activation (**D**).

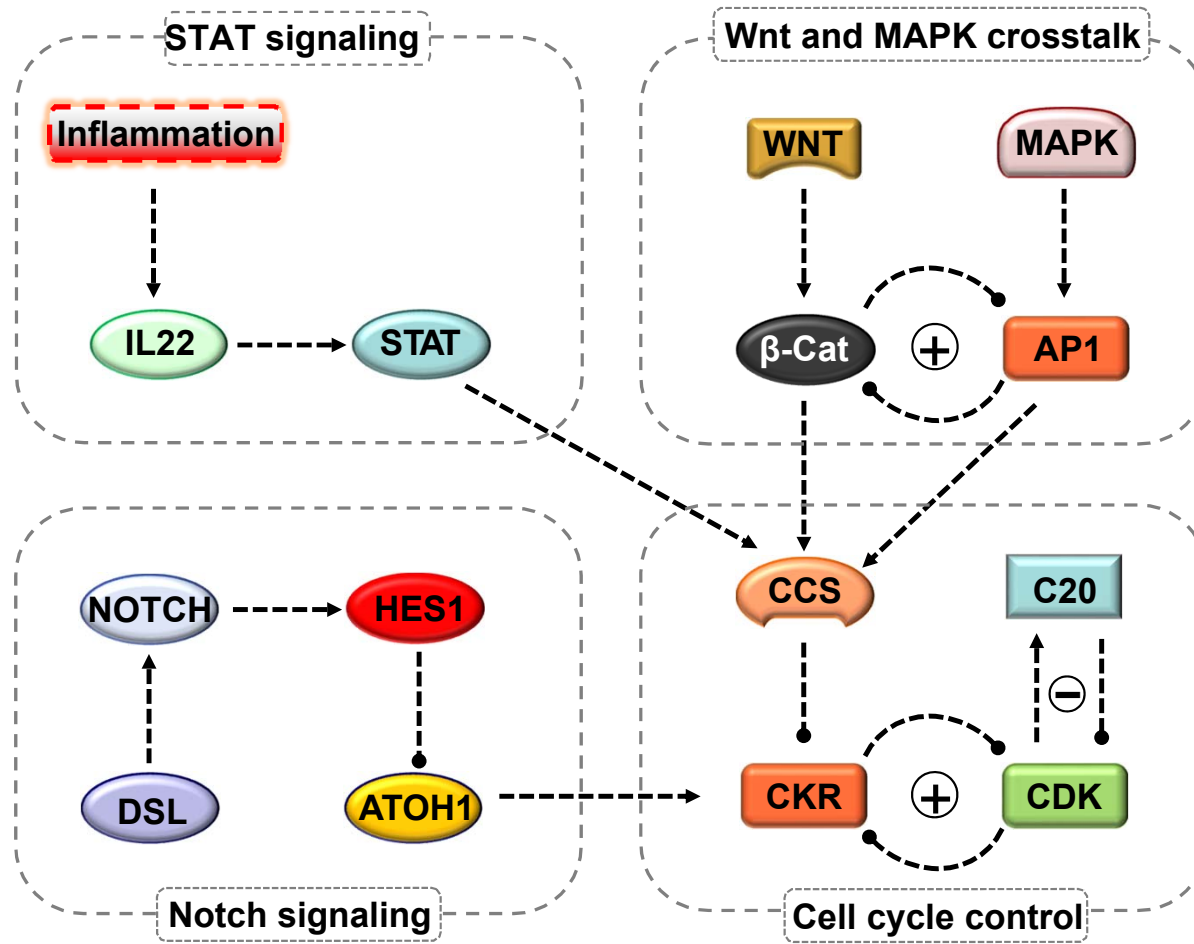
1. Wagers, A. J., and I. L. Weissman. 2004. Plasticity of adult stem cells. *Cell* 116(5):639-648.
2. Clevers, H. 2013. The intestinal crypt, a prototype stem cell compartment. *Cell* 154(2):274-284.
3. Noah, T. K., and N. F. Shroyer. 2013. Notch in the intestine: regulation of homeostasis and pathogenesis. *Annu Rev Physiol* 75:263-288.
4. Potten, C. S. 1986. Cell cycles in cell hierarchies. *Int J Radiat Biol Relat Stud Phys Chem Med* 49(2):257-278.
5. Schepers, A. G., R. Vries, M. van den Born, M. van de Wetering, and H. Clevers. 2011. Lgr5 intestinal stem cells have high telomerase activity and randomly segregate their chromosomes. *EMBO J* 30(6):1104-1109.
6. Stamatakis, D., M. Holder, C. Hodgetts, R. Jeffery, E. Nye, B. Spencer-Dene, D. J. Winton, and J. Lewis. 2011. Delta1 expression, cell cycle exit, and commitment to a specific secretory fate coincide within a few hours in the mouse intestinal stem cell system. *PLoS One* 6(9):e24484.
7. Coskun, M., M. Salem, J. Pedersen, and O. H. Nielsen. 2013. Involvement of JAK/STAT signaling in the pathogenesis of inflammatory bowel disease. *Pharmacol Res* 76:1-8.
8. Bruce Alberts, A. J., Julian Lewis, Martin Raff, Keith Roberts, and Peter Walter. 2002. *Molecular Biology of the Cell*, 4th edition. Garland Science, New York.
9. Batsivari, A., S. Rybtsov, C. Souilhol, A. Binagui-Casas, D. Hills, S. Zhao, P. Travers, and A. Medvinsky. 2017. Understanding Hematopoietic Stem Cell Development through Functional Correlation of Their Proliferative Status with the Intra-aortic Cluster Architecture. *Stem Cell Reports* 8(6):1549-1562.
10. Roccio, M., D. Schmitter, M. Knobloch, Y. Okawa, D. Sage, and M. P. Lutolf. 2013. Predicting stem cell fate changes by differential cell cycle progression patterns. *Development* 140(2):459-470.
11. Tyson, J. J., and B. Novak. 2010. Functional motifs in biochemical reaction networks. *Annu Rev Phys Chem* 61:219-240.
12. Mjolsness, E., D. H. Sharp, and J. Reinitz. 1991. A connectionist model of development. *J Theor Biol* 152(4):429-453.
13. Ballweg, R., F. Schozer, K. Elliott, A. Kuhn, L. Spotts, E. Aihara, and T. Zhang. 2017. Multiscale positive feedbacks contribute to unidirectional gastric disease progression induced by helicobacter pylori infection. *BMC Syst Biol* 11(1):111.
14. Ballweg, R., A. L. Paek, and T. Zhang. 2017. A dynamical framework for complex fractional killing. *Sci Rep* 7(1):8002.
15. Farin, H. F., I. Jordens, M. H. Mosa, O. Basak, J. Korving, D. V. Tauriello, K. de Punder, S. Angers, P. J. Peters, M. M. Maurice, and H. Clevers. 2016. Visualization of a short-range Wnt gradient in the intestinal stem-cell niche. *Nature* 530(7590):340-343.
16. Yang, Y. P., H. Ma, A. Starchenko, W. J. Huh, W. Li, F. E. Hickman, Q. Zhang, J. L. Franklin, D. P. Mortlock, S. Fuhrmann, B. D. Carter, R. A. Ihrie, and R. J. Coffey. 2017. A Chimeric Egfr Protein Reporter Mouse Reveals Egfr Localization and Trafficking In Vivo. *Cell Rep* 19(6):1257-1267.
17. Toni, T., D. Welch, N. Strelkowa, A. Ipsen, and M. P. Stumpf. 2009. Approximate Bayesian computation scheme for parameter inference and model selection in dynamical systems. *J R Soc Interface* 6(31):187-202.
18. Max Kuhn, K. J. 2016. *Applied Predictive Modeling* Springer, New York
19. Wiener, A. L. a. M. 2002. Classification and Regression by randomForest. *R News* 2(3):18.
20. Clevers, H., K. M. Loh, and R. Nusse. 2014. Stem cell signaling. An integral program for tissue renewal and regeneration: Wnt signaling and stem cell control. *Science* 346(6205):1248012.
21. Heuberger, J., F. Kosel, J. Qi, K. S. Grossmann, K. Rajewsky, and W. Birchmeier. 2014. Shp2/MAPK signaling controls goblet/paneth cell fate decisions in the intestine. *Proc Natl Acad Sci U S A* 111(9):3472-3477.

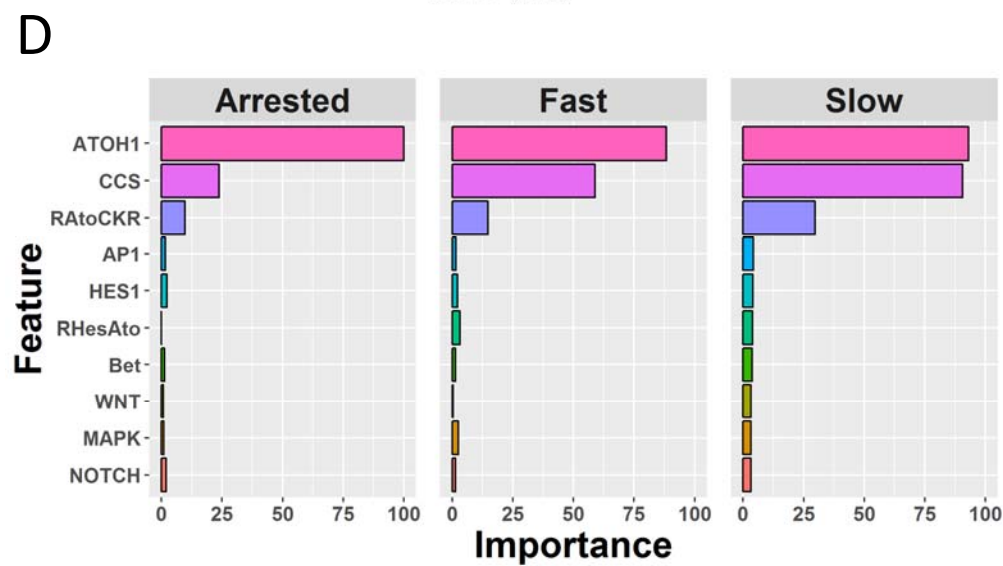
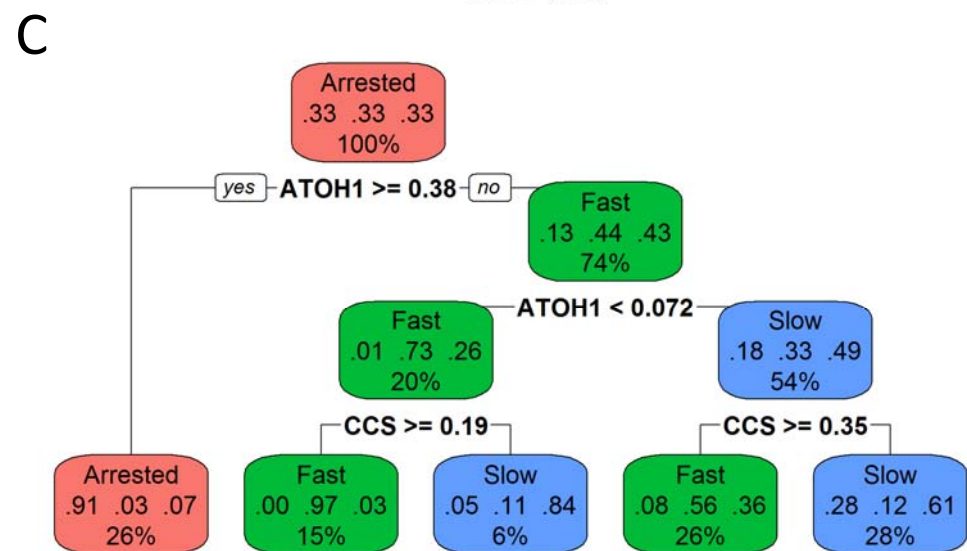
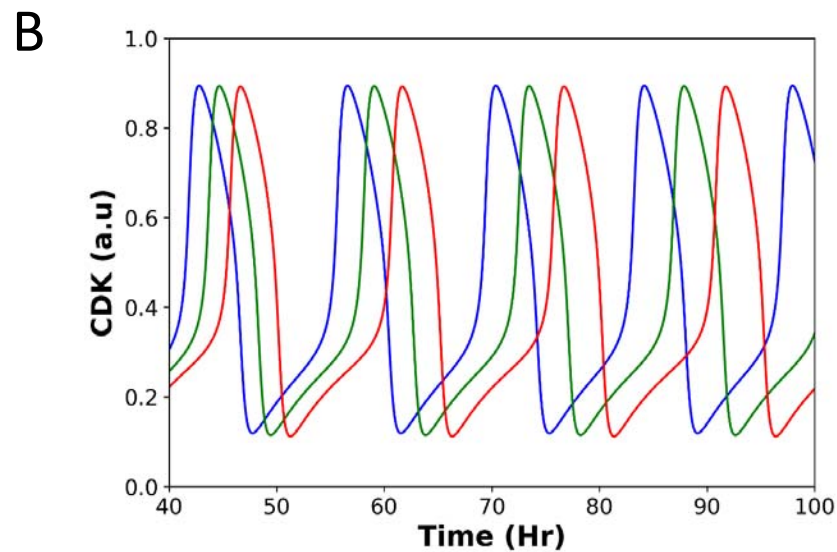
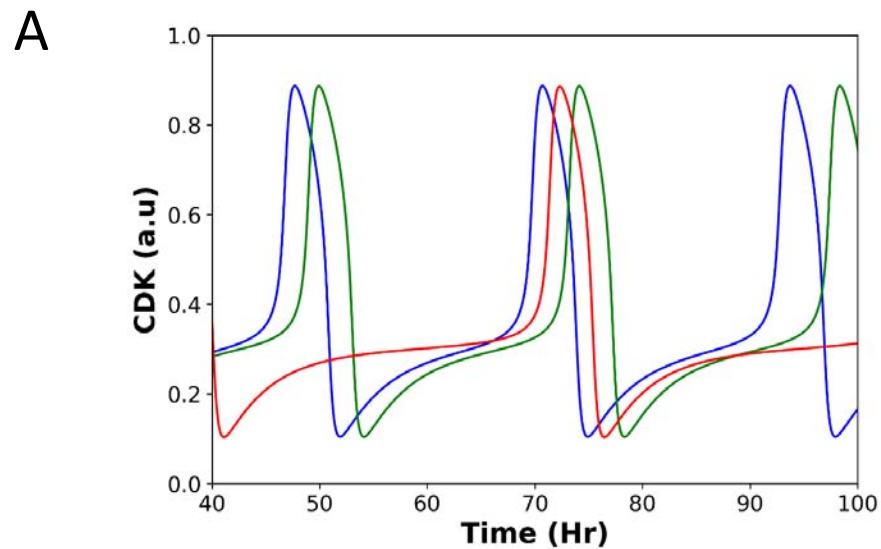
22. Riemer, P., A. Sreekumar, S. Reinke, R. Rad, R. Schafer, C. Sers, H. Blaker, B. G. Herrmann, and M. Morkel. 2015. Transgenic expression of oncogenic BRAF induces loss of stem cells in the mouse intestine, which is antagonized by beta-catenin activity. *Oncogene* 34(24):3164-3175.
23. Gilbert, S., H. Nivarthi, C. N. Mayhew, Y. H. Lo, T. K. Noah, J. Vallance, T. Rulicke, M. Muller, A. G. Jegga, W. Tang, D. Zhang, M. Helmrath, N. Shroyer, R. Moriggl, and X. Han. 2015. Activated STAT5 confers resistance to intestinal injury by increasing intestinal stem cell proliferation and regeneration. *Stem Cell Reports* 4(2):209-225.
24. Lindemans, C. A., M. Calafiore, A. M. Mertelsmann, M. H. O'Connor, J. A. Dudakov, R. R. Jenq, E. Velardi, L. F. Young, O. M. Smith, G. Lawrence, J. A. Ivanov, Y. Y. Fu, S. Takashima, G. Hua, M. L. Martin, K. P. O'Rourke, Y. H. Lo, M. Mokry, M. Romera-Hernandez, T. Cupedo, L. E. Dow, E. E. Nieuwenhuis, N. F. Shroyer, C. Liu, R. Kolesnick, M. R. van den Brink, and A. M. Hanash. 2015. Interleukin-22 promotes intestinal-stem-cell-mediated epithelial regeneration. *Nature* 528(7583):560-564.
25. Kazanjian, A., and N. F. Shroyer. 2011. NOTCH Signaling and ATOH1 in Colorectal Cancers. *Curr Colorectal Cancer Rep* 7(2):121-127.
26. Breiman, L. 1984. Classification and regression trees. Wadsworth International Group, Belmont, Calif.
27. Breiman, L. 2001. Random Forests. *Mach. Learn.* 45(1):5-32.
28. Date, S., and T. Sato. 2015. Mini-gut organoids: reconstitution of the stem cell niche. *Annu Rev Cell Dev Biol* 31:269-289.
29. Abe, T., A. Sakaue-Sawano, H. Kiyonari, G. Shioi, K. Inoue, T. Horiuchi, K. Nakao, A. Miyawaki, S. Aizawa, and T. Fujimori. 2013. Visualization of cell cycle in mouse embryos with Fucci2 reporter directed by Rosa26 promoter. *Development* 140(1):237-246.
30. Matsu-Ura, T., A. Dovzhenok, E. Aihara, J. Rood, H. Le, Y. Ren, A. E. Rosselot, T. Zhang, C. Lee, K. Obrietan, M. H. Montrose, S. Lim, S. R. Moore, and C. I. Hong. 2016. Intercellular Coupling of the Cell Cycle and Circadian Clock in Adult Stem Cell Culture. *Mol Cell* 64(5):900-912.
31. Bossuyt, W., A. Kazanjian, N. De Geest, S. Van Kelst, G. De Hertogh, K. Geboes, G. P. Boivin, J. Luciani, F. Fuks, M. Chuah, T. VandenDriessche, P. Marynen, J. Cools, N. F. Shroyer, and B. A. Hassan. 2009. Atonal homolog 1 is a tumor suppressor gene. *PLoS Biol* 7(2):e39.
32. Kuznetsov, Y. A. 2004. Elements of applied bifurcation theory. Springer, New York.
33. Cohen, J. E. 2004. Mathematics is biology's next microscope, only better; biology is mathematics' next physics, only better. *PLoS Biol* 2(12):e439.
34. Buske, P., J. Galle, N. Barker, G. Aust, H. Clevers, and M. Loeffler. 2011. A comprehensive model of the spatio-temporal stem cell and tissue organisation in the intestinal crypt. *PLoS Comput Biol* 7(1):e1001045.
35. Kay, S. K., H. A. Harrington, S. Shepherd, K. Brennan, T. Dale, J. M. Osborne, D. J. Gavaghan, and H. M. Byrne. 2017. The role of the Hes1 crosstalk hub in Notch-Wnt interactions of the intestinal crypt. *PLoS Comput Biol* 13(2):e1005400.
36. Du, H., Q. Nie, and W. R. Holmes. 2015. The Interplay between Wnt Mediated Expansion and Negative Regulation of Growth Promotes Robust Intestinal Crypt Structure and Homeostasis. *PLoS Comput Biol* 11(8):e1004285.
37. Zhang, L., A. D. Lander, and Q. Nie. 2012. A reaction-diffusion mechanism influences cell lineage progression as a basis for formation, regeneration, and stability of intestinal crypts. *BMC Syst Biol* 6:93.
38. Kershaw, S. K., H. M. Byrne, D. J. Gavaghan, and J. M. Osborne. 2013. Colorectal cancer through simulation and experiment. *IET Syst Biol* 7(3):57-73.
39. Alexander G. Fletcher, P. J. M., Philip K. Maini. 2015. Multiscale modelling of intestinal crypt

- organization and carcinogenesis. *Mathematical Models and Methods in Applied Sciences* 25(13):2563-2585.
40. Carulli, A. J., L. C. Samuelson, and S. Schnell. 2014. Unraveling intestinal stem cell behavior with models of crypt dynamics. *Integr Biol (Camb)* 6(3):243-257.
  41. Lloyd-Lewis, B., A. G. Fletcher, T. C. Dale, and H. M. Byrne. 2013. Toward a quantitative understanding of the Wnt/-catenin pathway through simulation and experiment. *Wires Syst Biol Med* 5(4):391-407.
  42. Ferrell, J. E., Jr. 2012. Bistability, bifurcations, and Waddington's epigenetic landscape. *Curr Biol* 22(11):R458-466.
  43. Csikasz-Nagy, A., D. Battogtokh, K. C. Chen, B. Novak, and J. J. Tyson. 2006. Analysis of a generic model of eukaryotic cell-cycle regulation. *Biophys J* 90(12):4361-4379.

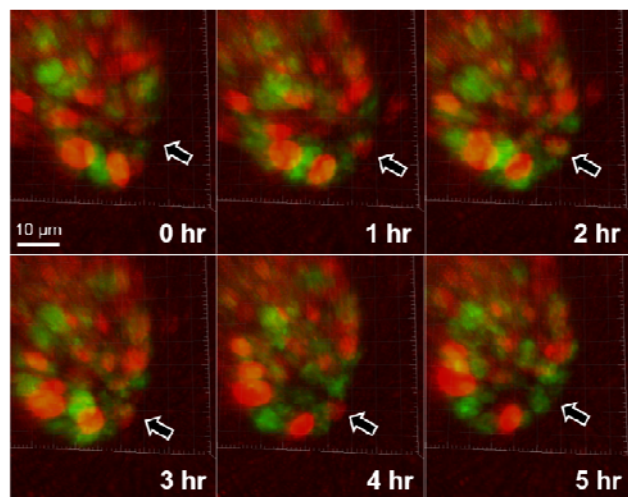


B

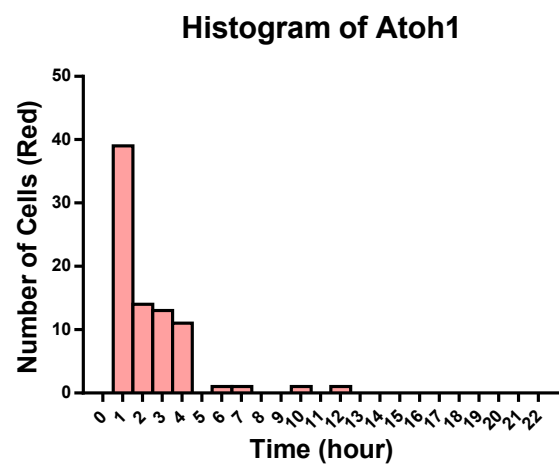




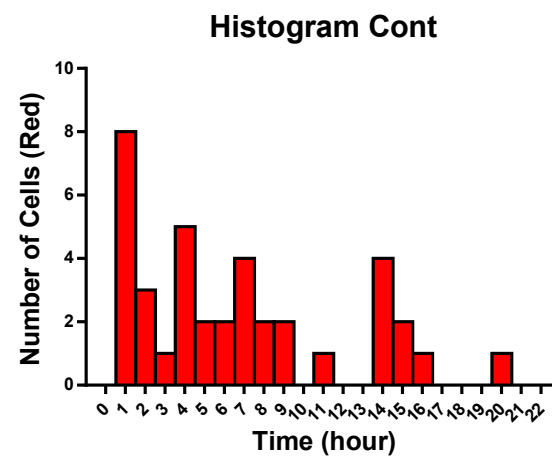
A



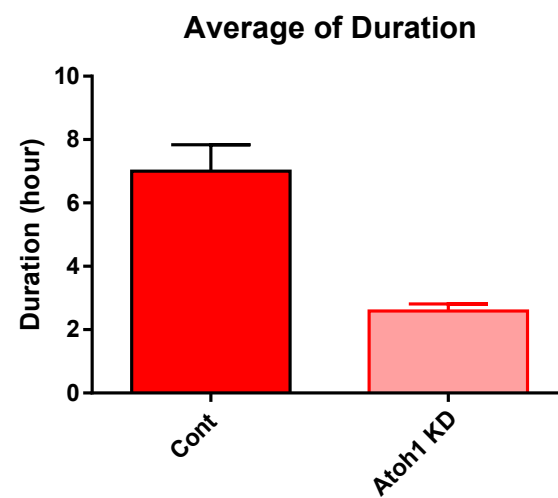
C

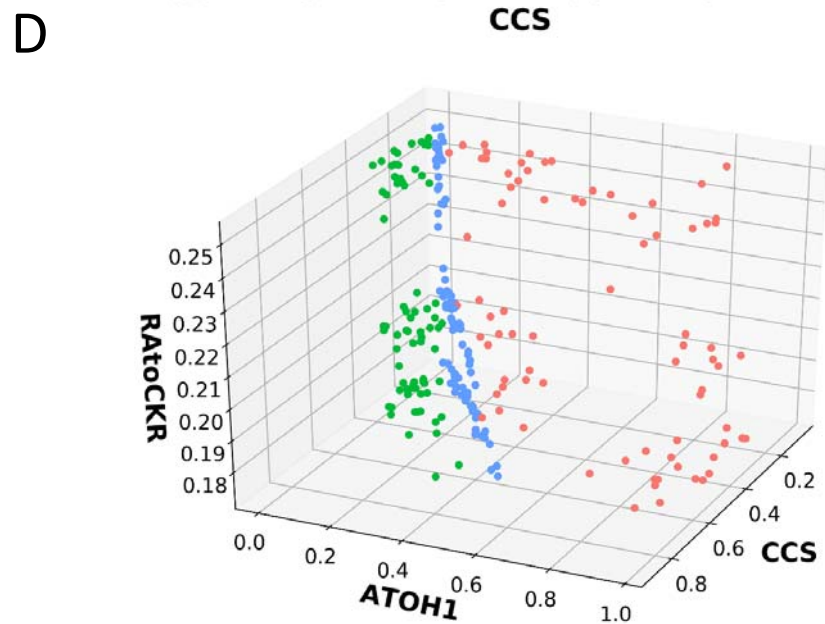
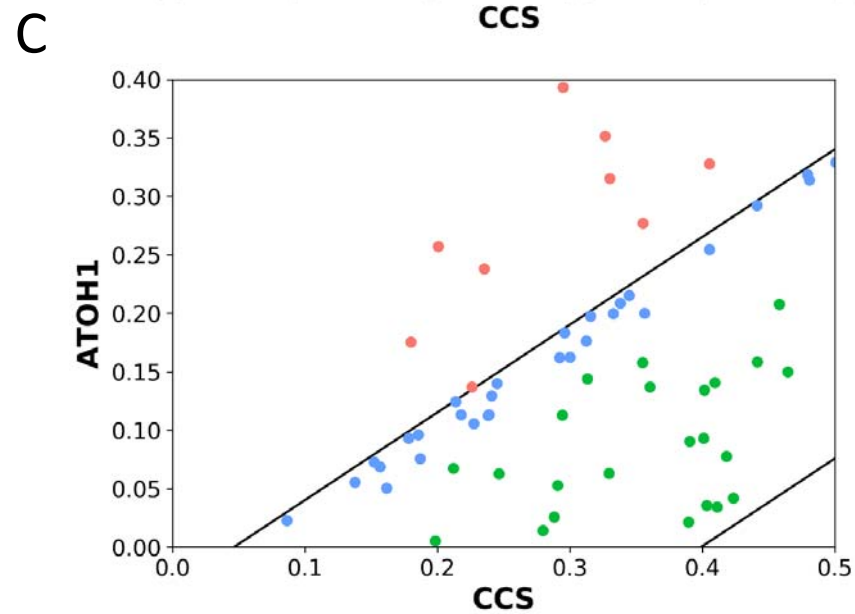
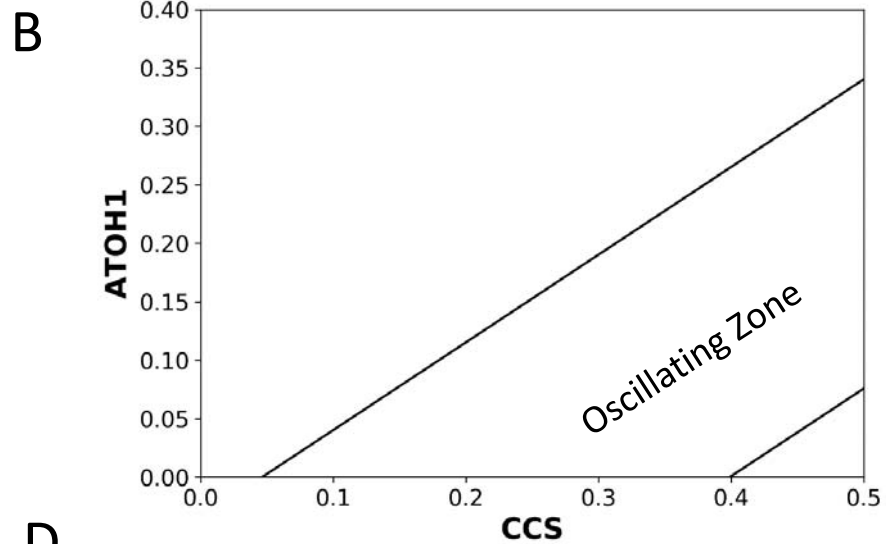
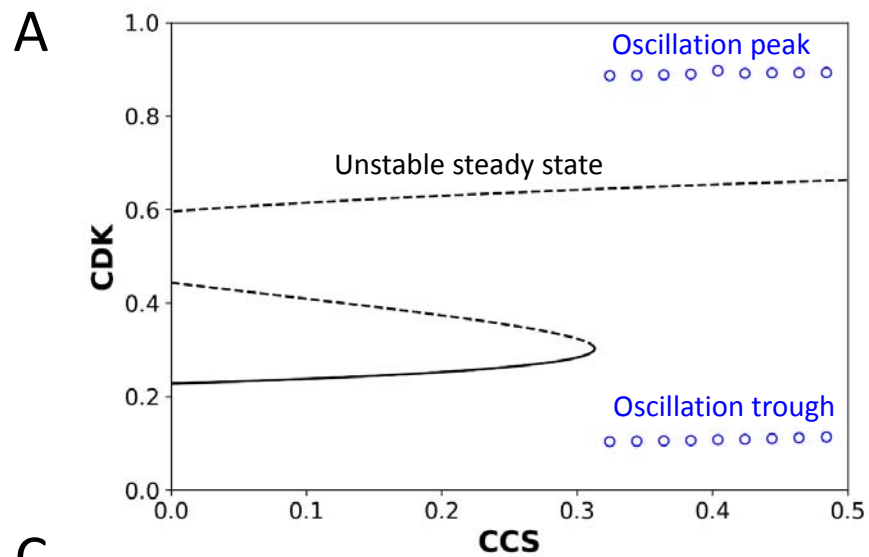


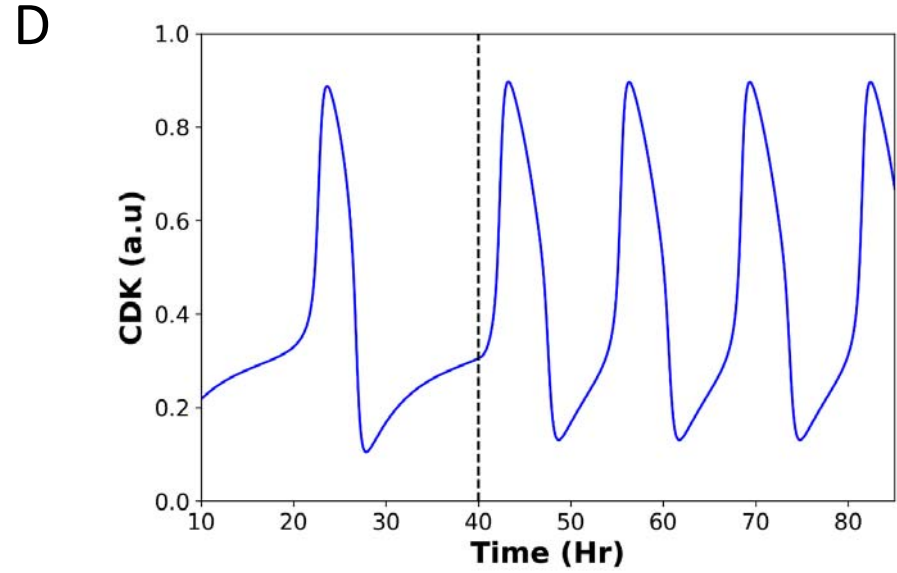
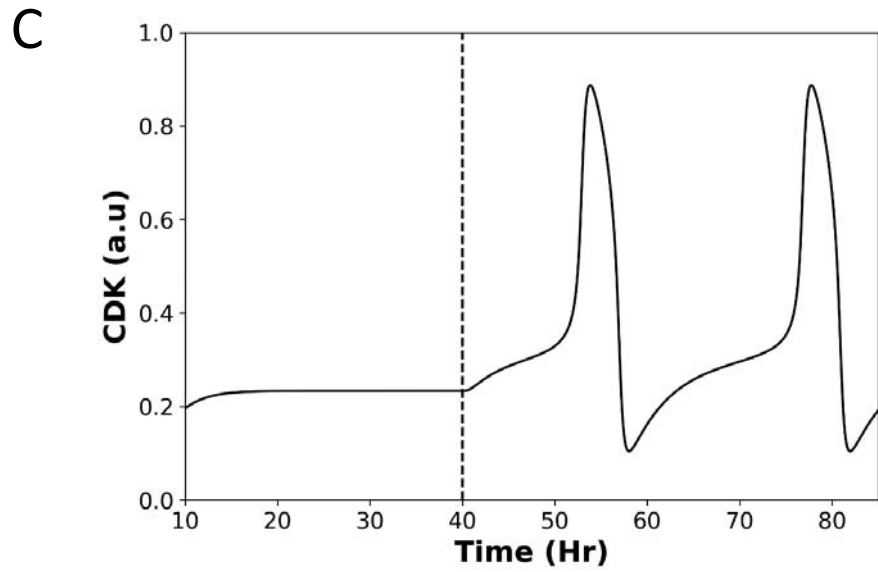
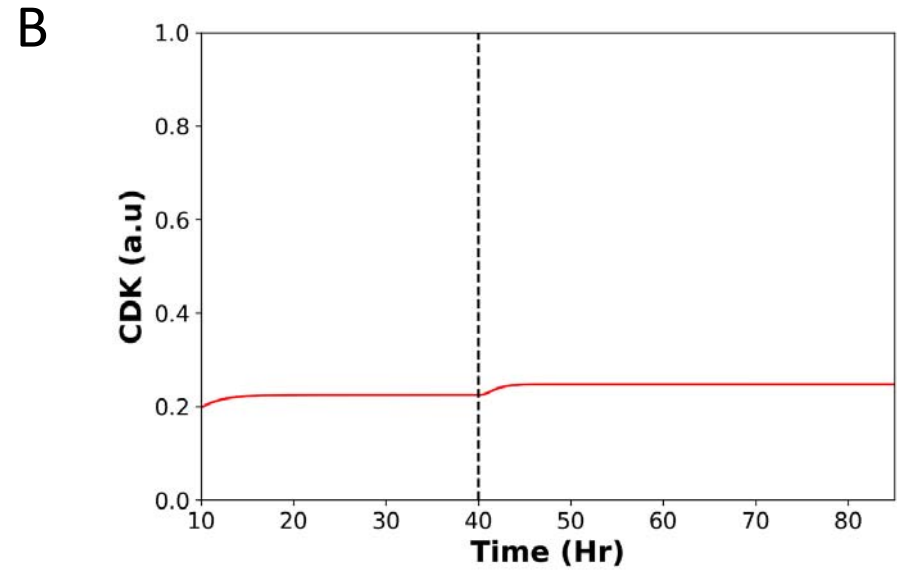
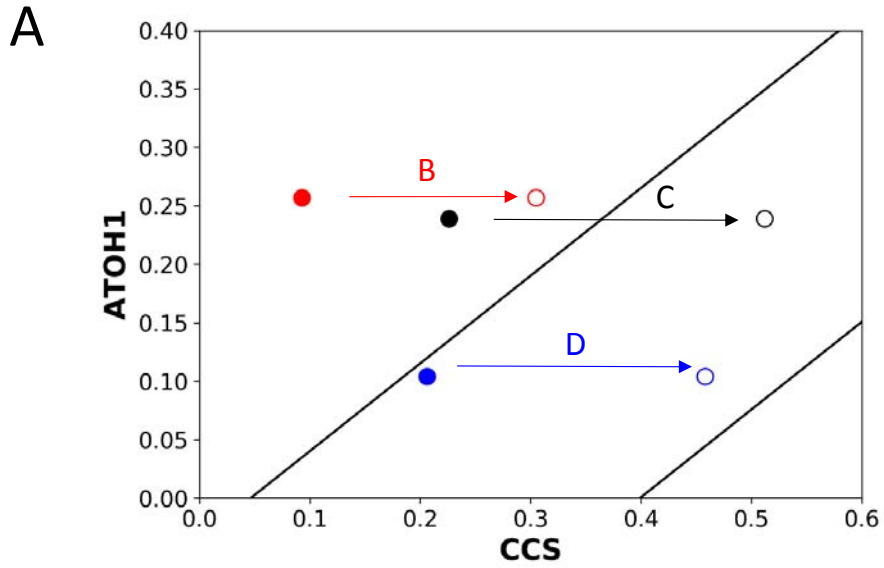
B



D







**Supplementary text and tables for the manuscript “*Unraveling the control of cell cycle periods during intestinal stem cell differentiation*”**

Richard Ballweg<sup>1</sup>, Lee, Suengwon<sup>1</sup>, Xiaonan Han<sup>2</sup>, Philip Maini<sup>3</sup>, Helen Byrne<sup>3</sup>, Christian Hong<sup>1</sup>, and Tongli Zhang<sup>1\*</sup>

**The four functional modules of the model.** The current model focuses on the control of proliferation of intestinal stem cells (ISCs) and their progeny, which maintain the epithelial lining of the intestine. The cell cycle module is at the core of our investigation. As elaborated below, Wnt, an essential niche signal provided by Paneth cells and the surrounding stroma, is required for sustained self-renewal of intestinal stem cells; Notch signaling provided by Paneth cells promotes cell proliferation; the STAT pathway is important for transducing inflammatory signals to the cell cycle machinery during diseases such as inflammatory bowel disease. All four modules are integrated in our model.

**The STAT signaling module.** In response to inflammatory signals, innate immune cells in the intestine are activated to secrete IL22 which, in turn, activates the STAT signaling pathway within intestinal epithelial cells (1). Activation of STAT enhances the production of Cyclin D and, thereby, the proliferation of ISCs. When the STAT pathway is inactivated, ISC proliferation is impaired, resulting in a weaker intestinal barrier and impaired damage repair (2). While in practice the STAT family comprises 7 different family members (3), in our model we represent them via a single, generic protein, STAT, which is activated by IL-22.

**The WNT and MAPK crosstalk module.** In their niches, ISCs are exposed to high levels of Wnt ligands produced by adjacent Paneth cells and the surrounding stromal cells (4-6). The canonical Wnt pathway is activated by the binding of these Wnt ligands to cell surface receptors,

which in turn stabilizes cytoplasmic  $\beta$ -catenin (7, 8). Stabilized  $\beta$ -catenin then translocates into the nucleus whereupon it activates the expression of down-stream genes (e.g. Cyclin D, c-Myc, Lgr5, and Ascl2). Of these target genes, both Cyclin D and c-Myc promote cell proliferation; in our model they are lumped together as Cell Cycle Starters (CCS). Upon ablation of  $\beta$ -catenin, ISC proliferation is blocked and the stem cell pool is lost (6).

Cyclin D (bound to Cdk4/6) actively sequesters Cdk inhibitors such as p27 and p57. In addition, the Cyclin D:Cdk complex phosphorylates and inactivates Rb, which then promotes the activation of the transcription factor E2F and the transcription of Cyclin E and Cyclin A. After E2F is activated, it also induces the transcription of the APC:Cdh1 inhibitor Emi1.

The Mitogen Activated Protein Kinase (MAPK) pathway also promotes cell cycle progression. Activated MAPK phosphorylates and activates the transcription factor Activator protein 1 (AP1), and promotes the production of Cyclin D (9).

In contrast to Wnt signaling, MAPK signaling is weakest at the bottom of the intestinal crypt and increases with distance from the crypt base (10). The MAPK pathway is known to repress the transcriptional activity of the Wnt signaling pathway by decreasing the active form of Tcf4 (an essential transcriptional partner of nuclear  $\beta$ -catenin) (10). When MAPK signaling is inhibited, levels of active Tcf4 isoforms increase, and hence, the levels of nuclear  $\beta$ -catenin bound to active Tcf4 isoforms increase (10). Consistent with these observations, it has been hypothesized that the transcription programs downstream of the MAPK and Wnt-  $\beta$ -catenin pathways may repress each other (11). On the basis of these reports, the current model incorporates a mutual repression between the transcriptional activities of the MAPK and Wnt signaling pathways, this repression

behavior is modelled by assuming that AP-1 and  $\beta$ -catenin inhibit the rate at which the other protein is produced (see **Table 1**).

**The Notch signaling module.** Four types of Notch receptors and several ligands Delta-like (Dll), Serrate, Lag-2 (DSLs) are functional in mammalian cells (12). Among these, the ligands Dll1 and Dll4 (13), and the receptors Notch1 and Notch2 (14), play significant roles in the intestine. In our model, we denote by Notch the combined activity of Notch1 and Notch2, and by DSL the net effect of Dll1 and Dll4. We assume further that DSL activates Notch.

Upon binding to DSL ligands, the Notch receptor is elevated by the  $\Upsilon$ -secretase enzyme complex, causing the release of the Notch intracellular domain (NICD), which then translocates into the nucleus. Although NICD does not have transcriptional activity, it can recruit transcriptional activators to the DNA binding complex CSL (CBF1, Suppressor of Hairless, Lag-1). Through CSL, NICD promotes the expression of Notch target genes, including Hes1. In our model, we assume that Notch activates Hes1 production. Hes1 is a basic helix-loop-helix transcriptional repressor, which represses the transcription factor Atoh1 (15). When active, Atoh1 drives stem cells towards a secretory cell fate in the intestine by activating several downstream genes (16). Atoh1 is known to be necessary for expression of the CDK inhibitors p27 and p57 during Notch inhibition (17). Atoh1 has also been shown to induce expression of p21, p27 and p57 in colorectal cancer cell lines (18). While Hes1 has been shown to directly inhibit p27 and p57, in keeping with the minimal nature of the model, and due to Atoh1's role in differentiation, we choose to omit this reaction from our model.

**The cell proliferation module.** Many mathematical models of varying detail have been constructed for the control of the mammalian cell cycle (19-24). Because the current work focuses on how differentiation interacts with the cell cycle control mechanism, rather than the

detailed molecular interactions within the cell cycle control network, we employ an idealized model of cell cycle control.

Cell proliferation is driven by the periodic activation and inactivation of Cyclin-dependent kinases (CDK) (25). In non-proliferating cells, CDK is kept inactive by several layers of regulation. CDK inhibitors are abundant in resting cells, binding to CDKs and preventing them from reaching their physiological targets. Also, the transcriptional repressor RB is active and represses the transcription of Cyclins A and E, which are the activating partners of CDK. Meanwhile, the degradation machinery of APC/C:Cdh1 causes the degradation of CDK activating cyclins (25). These repressors of CDK are lumped together as CKR in the current model.

CDK actively inhibits its repressors. It phosphorylates inhibitors such as p27, which degrade more rapidly when they are phosphorylated. Activated CDK also phosphorylates Rb and inactivates Rb (25). Additionally, CDK phosphorylates the APC/C protein complex preventing it from binding to Cdh1, thus blocking activation of the APC/C:Cdh1 degradation machinery (25). In this way, CDK and its repressor, CKR, form a mutually antagonistic positive feedback loop. This positive feedback is incorporated in the current model.

The current cell cycle module also incorporated a negative feedback loop, in which CDK activates the degradation machinery APC/C:Cdc20. By degrading cyclins, which are essential activating partners of CDK, APC/C:Cdc20 causes inactivation of CDK (25).

**Supplementary Table 1. Equations of the model**

The Notch Signalling Module	
HES1	NOTCH
Activity of the transcription repressor Hes1	Activity of the Notch pathway
$\frac{dHES}{dt} = \tau_{HES} \cdot (F_{HES} - HES)$	$\frac{dNOC}{dt} = \tau_{NOC} \cdot (F_{NOC} - NOC)$
$F_{HES} = \frac{1}{1 + e^{-\sigma \cdot W_{HES}}}$	$F_{NOC} = \frac{1}{1 + e^{-\sigma \cdot W_{NOC}}}$
$W_{HES} = R_0^{HES} + R_{NOC}^{HES} \cdot NOC$	$W_{NOC} = R_0^{NOC} + R_{DSL}^{NOC} * DSL$
ATOH1	
Activity of Atoh1	
$\frac{dAtoh1}{dt} = \tau_{Atoh1} \cdot (F_{Atoh1} - Atoh1)$	
$F_{Atoh1} = \frac{1}{1 + e^{-\sigma \cdot W_{Atoh1}}}$	
$W_{Atoh1} = R_0^{Atoh1} + R_{Hes}^{Atoh1} \cdot Hes$	
The Stat Signalling Module	
Activity of STAT transcription factors	
$\frac{dStat}{dt} = \tau_{stat} \cdot (F_{Stat} - Stat)$	
$F_{Stat} = \frac{1}{1 + e^{-\sigma \cdot W_{Stat}}}$	
$W_{Stat} = R_0^{Stat} + R_{Il22}^{Stat} \cdot Il22$	
The Wnt-MAPK Module	
BET	AP1
Activity of the transcription activator $\beta$ -catenin of the Wnt pathway	Activation of the transcription factor AP1 of the MAPK pathway
$\frac{dBET}{dt} = \tau_{BET} \cdot (F_{BET} - BET)$	$\frac{dAP1}{dt} = \tau_{AP1} \cdot (F_{AP1} - AP1)$
$F_{BET} = \frac{1}{1 + e^{-\sigma \cdot W_{BET}}}$	$F_{AP1} = \frac{1}{1 + e^{-\sigma \cdot W_{AP1}}}$
$W_{BET} = R_0^{BET} + R_{Wnt}^{BET} \cdot Wnt + R_{AP1}^{BET} \cdot AP1$	$W_{AP1} = R_0^{AP1} + R_{MAPK}^{AP1} \cdot MAPK + R_{BET}^{AP1} \cdot BET$
The Cell Cycle Module	
CKR	CDK
CDK repressors	Cyclin dependent kinases
$\frac{dCKR}{dt} = \tau_{CKR} \cdot (F_{CKR} - CKR)$	$\frac{dCDK}{dt} = \tau_{CDK} \cdot (F_{CDK} - CDK)$
$F_{CKR} = \frac{1}{1 + e^{-\sigma \cdot W_{CKR}}}$	$F_{CDK} = \frac{1}{1 + e^{-\sigma \cdot W_{CDK}}}$
$W_{CKR} = R_0^{CKR} + R_{CDK}^{CKR} \cdot CDK + R_{CCS}^{CKR} \cdot CCS + R_{Atoh1}^{CKR} \cdot Atoh1$	$W_{CDK} = R_0^{CDK} + R_{CKR}^{CDK} \cdot CKR + R_{C20}^{CDK} \cdot C20$
C20	CCS
APC/C:Cdc20 degradation machinery	Cell cycle starters
$\frac{dC20}{dt} = \tau_{C20} \cdot (F_{C20} - C20)$	$\frac{dCCS}{dt} = k_{sBET} \cdot BET + k_{sAP1} \cdot AP1 + k_{sStat} \cdot Stat - k_{dCCS} \cdot CCS$
$F_{C20} = \frac{1}{1 + e^{-\varepsilon \cdot W_{C20}}}$	
$W_{NOC} = R_0^{C20} + R_{CDK}^{C20} \cdot CDK$	

**Supplementary Table 2. Basal parameters of the model**

Model Parameters			
Parameters for Notch Signalling module			
Time scale of Hes1	Hes1 background inactivation	Time scale of Notch	Notch background inactivation
$\tau_{HES} = 5$	$R_0^{HES} = -0.6$	$\tau_{NOC} = 5$	$R_0^{NOC} = -0.7$
Nonlinearity adjusting factor	Activation of Hes1 by Notch pathway	Activation of notch pathway by Dsl ligands	
$\sigma = 5$	$R_{NOC}^{HES} = 1$	$R_{DSL}^{NOC} = 1.5$	
Atoh1 background activation	Inactivation of Atoh1 by Hes1	Time scale of Atoh1	
$R_0^{Atoh1} = 0.6$	$R_{Hes}^{Atoh1} = -1.2$	$\tau_{Atoh1} = 5$	
Parameters for Stat Signalling Module			
IL22 Level	Stat background inactivation	Stat activation by IL-22	
$IL22 = 1$	$R_0^{Stat} = -0.7$	$R_{IL22}^{Stat} = 1.5$	
Parameters for Wnt-MAPK module			
Time scale of $\beta$ -catenin	$\beta$ -catenin background inactivation	Time scale of AP1	AP1 background inactivation
$\tau_{Bet} = 100$	$R_0^{BET} = -0.2$	$\tau_{Ap1} = 100$	$R_0^{AP1} = -1$
Activation of $\beta$ -catenin by Wnt pathway	Inhibition of $\beta$ -catenin by AP1	Activation of AP1 by MAPK pathway	Inactivation of AP1 by $\beta$ -catenin
$R_{Wnt}^{BET} = 0.9$	$R_{AP1}^{BET} = -1.2$	$R_{MAPK}^{AP1} = 2$	$R_{BET}^{AP1} = -1.5$
Parameters for cell cycle module			
Time scale of CKR	CKR background activation	Time scale of CDK	CDK background activation
$\tau_{CKR} = 5$	$R_0^{CKR} = 1.03$	$\tau_{CDK} = 5$	$R_0^{CDK} = 0.68$
Activation of CKR by Atoh1	Inhibition of CKR by CDK	Inhibition of CDK by CKR	Inhibition of CDK by C20
$R_{Ato}^{CKR} = 0.23$	$R_{CDK}^{CKR} = -1.5$	$R_{CKR}^{CDK} = -1$	$R_{C20}^{CDK} = -0.5$
Time scale of C20	Inhibition of CKR by CCS	Promotion by $\beta$ -catenin	CCS degradation
$\tau_{c20} = 0.5$	$R_{CCS}^{CKR} = -0.15$	$k_{sBET} = 0.28$	$k_{dCCS} = 1$
Activation of C20 by CDK	C20 background inactivation	Promotion by AP1	Nonlinearity adjusting factor
$R_{CDK}^{C20} = 1.1$	$R_0^{C20} = -0.7$	$k_{sAP1} = 0.5$	$\varepsilon = 15$
Nonlinearity adjusting factor	Promotion by Stat		
$\sigma = 5$	$k_{sStat} = 0.28$		

## Supplementary Figure Legends:

### Supplementary Figure 1.

An example of a fully filled Classification Tree for a total of 300 cells were. Nodes are labeled Slow, Fast or Arrested based on the dominant cell type.

### Supplementary Figure 2.

Classification Trees generated with different ranges of parameter variability and different numbers of models, this figure accompanies **Figure 2C** of the main text. **A.** Variability: 70% to 130%, 3000 models. **B.** Variability: 70% to 130% 10,000 cells. **C.** Variability: 50% to 200% ~10,000 cells. **D.** Variability: 20% to 500% 10,000 cells. Nodes are labeled Slow, Fast or Arrested based on the dominating cell type.

### Supplementary Figure 3.

Variable importance analysis with Random Forest, computed with different ranges of parameter variability and different numbers of models. This accompanies **Figure 2D** of the main text. **A.** Variability: 70% to 130%, 3000 models. **B.** Variability: 70% to 130% 10,000 models. **C.** Variability: 50% to 200%, ~10,000 models. **D.** Variability: 20% to 500% , ~10,000 models.

### Supplementary Figure 4

**A.** Period diagram depicting the change in cell cycle period (in hours) as a function of CCS; accompanies **Figure 4A** of the main text. **B.** Full 1 parameter bifurcation diagram with CDK as the representative variable and CCS as the control variable. A SNIC bifurcation and a Hopf Bifurcation are separated by an unstable, oscillatory region; accompanies **Figure 4A** of the main text.

## Supplementary Figure 5

2-D plot showing how the locations of the SNIC boundaries change as  $R_{Ato}^{CKR}$  varies ( $R_{Ato}^{CKR} = 0.175$  , Red;  $R_{Ato}^{CKR} = 0.20$  , Black;  $R_{Ato}^{CKR} = 0.25$  , Green) ; accompanies **Figures 4C** and **4D** of the main text.

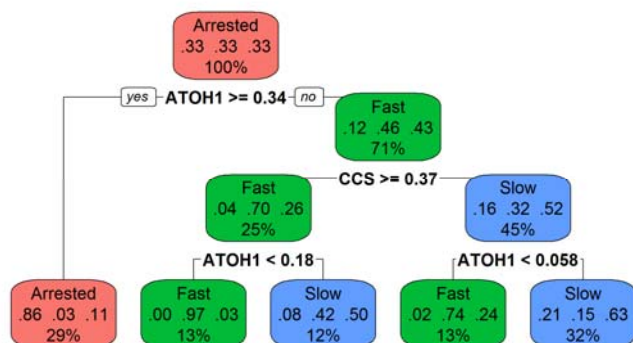
## REFERENCES

1. Lindemans CA, *et al.* (2015) Interleukin-22 promotes intestinal-stem-cell-mediated epithelial regeneration. *Nature* 528(7583):560-564.
2. Gilbert S, *et al.* (2015) Activated STAT5 confers resistance to intestinal injury by increasing intestinal stem cell proliferation and regeneration. *Stem Cell Reports* 4(2):209-225.
3. Shuai K & Liu B (2003) Regulation of JAK-STAT signalling in the immune system. *Nat Rev Immunol* 3(11):900-911.
4. Clevers H (2013) The intestinal crypt, a prototype stem cell compartment. *Cell* 154(2):274-284.
5. Crosnier C, Stamatakis D, & Lewis J (2006) Organizing cell renewal in the intestine: stem cells, signals and combinatorial control. *Nat Rev Genet* 7(5):349-359.
6. Fevr T, Robine S, Louvard D, & Huelsken J (2007) Wnt/beta-catenin is essential for intestinal homeostasis and maintenance of intestinal stem cells. *Mol Cell Biol* 27(21):7551-7559.
7. Clevers H, Loh KM, & Nusse R (2014) Stem cell signaling. An integral program for tissue renewal and regeneration: Wnt signaling and stem cell control. *Science* 346(6205):1248012.
8. Clevers H & Nusse R (2012) Wnt/beta-catenin signaling and disease. *Cell* 149(6):1192-1205.
9. Wilkinson MG & Millar JB (2000) Control of the eukaryotic cell cycle by MAP kinase signaling pathways. *FASEB J* 14(14):2147-2157.
10. Heuberger J, *et al.* (2014) Shp2/MAPK signaling controls goblet/paneth cell fate decisions in the intestine. *Proc Natl Acad Sci U S A* 111(9):3472-3477.
11. Riemer P, *et al.* (2015) Transgenic expression of oncogenic BRAF induces loss of stem cells in the mouse intestine, which is antagonized by beta-catenin activity. *Oncogene* 34(24):3164-3175.
12. Kopan R (2012) Notch signaling. *Cold Spring Harb Perspect Biol* 4(10).
13. Pellegrinet L, *et al.* (2011) Dll1- and dll4-mediated notch signaling are required for homeostasis of intestinal stem cells. *Gastroenterology* 140(4):1230-1240 e1231-1237.
14. Wu Y, *et al.* (2010) Therapeutic antibody targeting of individual Notch receptors. *Nature* 464(7291):1052-1057.
15. Kazanjian A & Shroyer NF (2011) NOTCH Signaling and ATOH1 in Colorectal Cancers. *Curr Colorectal Cancer Rep* 7(2):121-127.

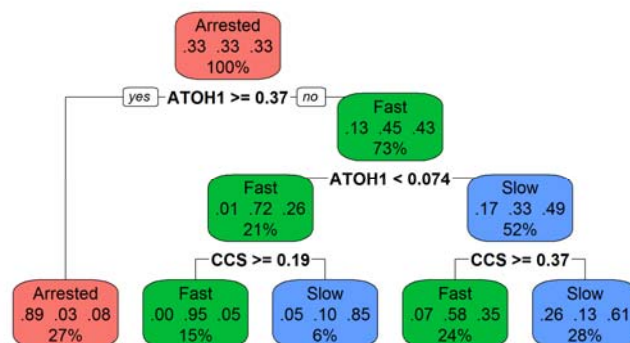
16. Noah TK & Shroyer NF (2013) Notch in the intestine: regulation of homeostasis and pathogenesis. *Annu Rev Physiol* 75:263-288.
17. Kim TH & Shivdasani RA (2011) Genetic evidence that intestinal Notch functions vary regionally and operate through a common mechanism of Math1 repression. *J Biol Chem* 286(13):11427-11433.
18. Bossuyt W, *et al.* (2009) Atonal homolog 1 is a tumor suppressor gene. *PLoS Biol* 7(2):e39.
19. Novak B & Tyson JJ (2004) A model for restriction point control of the mammalian cell cycle. *J Theor Biol* 230(4):563-579.
20. Csikasz-Nagy A, Battogtokh D, Chen KC, Novak B, & Tyson JJ (2006) Analysis of a generic model of eukaryotic cell-cycle regulation. *Biophys J* 90(12):4361-4379.
21. Gerard C & Goldbeter A (2009) Temporal self-organization of the cyclin/Cdk network driving the mammalian cell cycle. *Proc Natl Acad Sci U S A* 106(51):21643-21648.
22. Toettcher JE, *et al.* (2009) Distinct mechanisms act in concert to mediate cell cycle arrest. *Proc Natl Acad Sci U S A* 106(3):785-790.
23. Singhanian R, Sramkoski RM, Jacobberger JW, & Tyson JJ (2011) A hybrid model of mammalian cell cycle regulation. *PLoS Comput Biol* 7(2):e1001077.
24. Weis MC, Avva J, Jacobberger JW, & Sreenath SN (2014) A data-driven, mathematical model of mammalian cell cycle regulation. *PLoS One* 9(5):e97130.
25. Morgan DO (2007) *The cell cycle : principles of control* (Published by New Science Press in association with Oxford University Press ;  
Distributed inside North America by Sinauer Associates, Publishers, London  
Sunderland, MA) pp xxvii, 297 p.



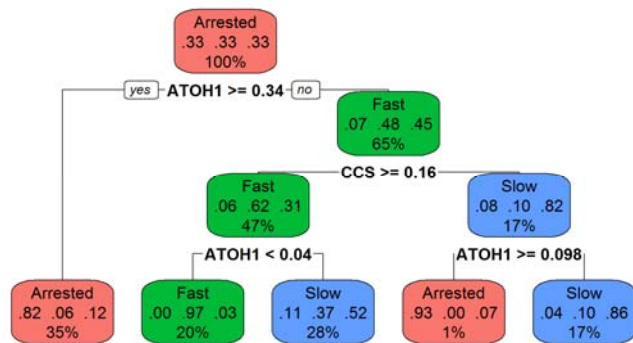
A



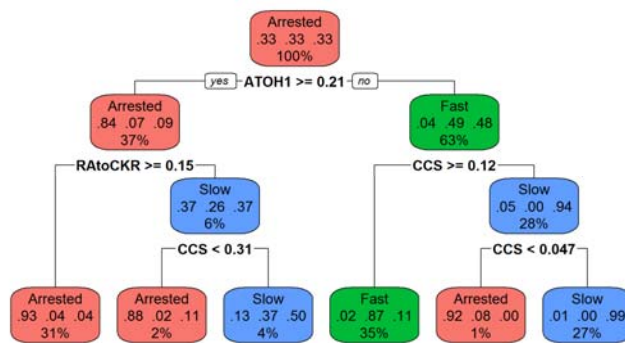
B



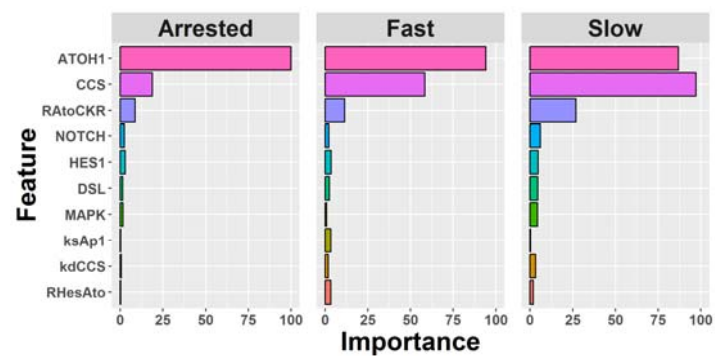
C



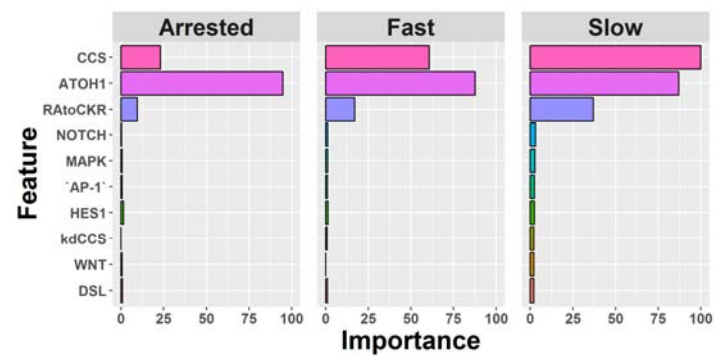
D



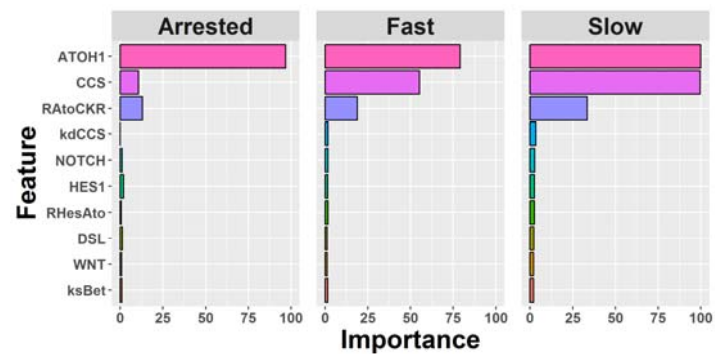
A



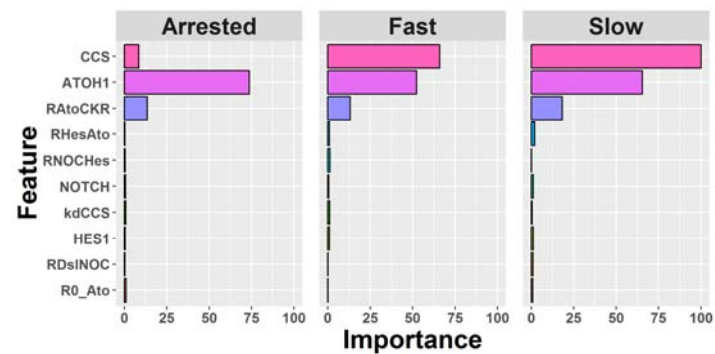
B

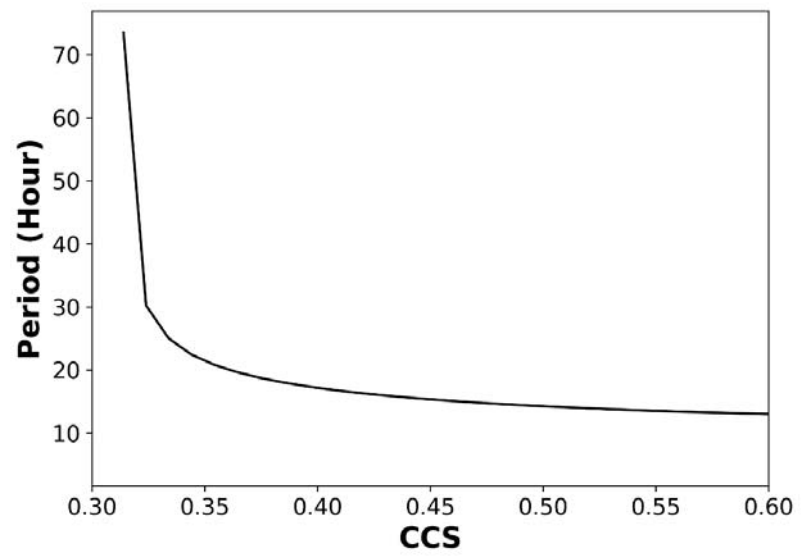


C



D



**A****B**